iScience

CellPress
OPEN ACCESS

Article

Synergistic effect between transition metal single atom and SnS_2 toward deep CO_2 reduction

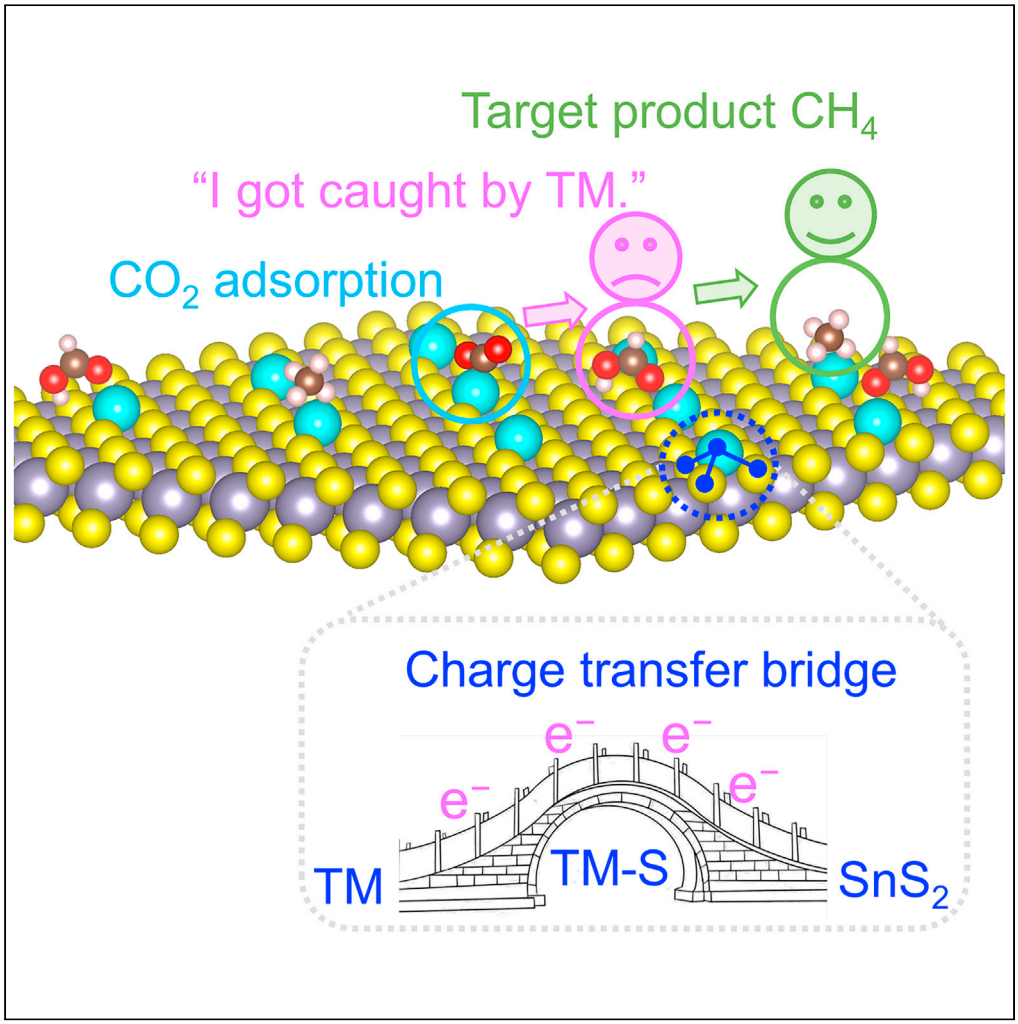

Yuehua Kong, Junhui Pan, Yi Li, Yongfan Zhang, Wei Lin

zhangyf@fzu.edu.cn (Y.Z.)
wlin@fzu.edu.cn (W.L.)

Highlights

The relationships among the configuration, energy, and electronic properties of TM@SnS_2 for CO_2 reduction are explored by using density functional theory

The "charge transfer bridge" promotes the adsorption of CO_2 on TM@SnS_2, thus enhancing the binding of HCOOH* to the catalyst for further hydrogenation and reduction to CH_4

The binding free energy of COOH* on TM@SnS_2 forms a "volcano curve" with the limiting potential of CO_2 reduction to CH_4

Kong et al., iScience 27, 109658
May 17, 2024
https://doi.org/10.1016/j.isci.2024.109658

iScience

CellPress
OPEN ACCESS

Article

Synergistic effect between transition metal single atom and SnS_2 toward deep CO_2 reduction

Yuehua Kong,[1] Junhui Pan,[1] Yi Li,[1,2] Yongfan Zhang,[1,2,*] and Wei Lin[1,2,3,*]

SUMMARY

The electrochemical reduction of CO_2 is an efficient channel to facilitate energy conversion, but the rapid design and rational screening of high-performance catalysts remain a great challenge. In this work, we investigated the relationships between the configuration, energy, and electronic properties of SnS_2 loaded with transition metal single atom (TM@SnS_2) and analyzed the mechanism of CO_2 activation and reduction by using density functional theory. The "charge transfer bridge" promoted the adsorption of CO_2 on TM@SnS_2, thus enhancing the binding of HCOOH* to the catalyst for further hydrogenation and reduction to high-value CH_4. The research revealed that the binding free energy of COOH* on TM@SnS_2 formed a "volcano curve" with the limiting potential of CO_2 reduction to CH_4, and the TM@SnS_2 (TM = Cr, Ru, Os, and Pt) at the "volcano top" exhibited a high CH_4 activity.

INTRODUCTION

Excessive emissions of CO_2 can bring about various environmental problems such as the greenhouse effect,[1,2] and its transformation into industrial feedstocks such as HCOOH and CH_4 by chemical methods is significant for climate change as well as sustainable development of energy.[3–5] However, the C=O bond energy of CO_2 is as up to 803 kJ mol^{-1}, which is highly inert to the extent that it is hard to be activated and requires the involvement of catalysts.[6] With mild reaction conditions and high conversion efficiency, electrochemical reduction is a cost-effective conversion approach.[7–9] And selectivity and limiting potential are two key dimensions of theoretical electrocatalysis research.[9] Transition metal (TM) single-atom catalysts have the advantages of small size and high activity, and their rational design and screening can help facilitate efficient and highly selective targeting of product generation, which has vital investigative implications for the pioneering of CO_2 electroreduction (CO_2ER).[10–13]

Earth-abundant and highly stable SnS_2 has been extensively studied in the CO_2ER. Unlike some TMX_n (X = S, Se, Te) and other ferromagnetic materials,[14] the highly symmetric nonpolar surface of 1T-SnS_2 makes the activation of linear CO_2 extremely challenging, and the products are therefore mostly confined to 2e HCOOH, which cannot be deeply reduced, and inevitably have by-products such as CO and H_2 generated.[15–18] Combined with our calculations, CO_2 is weakly adsorbed on pure SnS_2 (−0.15 eV) and is indeed not effectively activated by hydrogenation. Currently, the catalysts for the reduction of CO_2 to hydrocarbon products are mainly Cu-based materials with a limiting potential of −0.74 V vs. RHE for the reduction to CH_4, which is poorly selective, and the presence of multi-carbon hydrocarbon products.[19,20] However, the loaded TM can supply an independent active site for CO_2ER on the one hand, which ensures the C1 product selectivity, and strengthen the coupling between the highly polarized catalyst and the intermediate, thereby ensuring the selectivity of the multi-electron products. We envision that firstly catalyst reduces CO_2 to HCOOH, which is difficult to desorb under the action of TM and further hydrogenated deeply to create $CH(OH)_2$*, CH_2OOH*, or HCO* + H_2O(g) until the formation of multi-electron products, which greatly promotes the electron efficiency.

In this study, the CO_2ER activity of TM loaded in SnS_2 (TM@SnS_2, TM detailed in Figure 1) was investigated using first-principle methods. We firstly studied the relationship between the configuration, energy, and electronic properties of the catalysts constructed by different TMs and reasonably predicted their activation and catalytic performance; then, we proposed the concept of "charge transfer bridge" and fully confirmed this conjecture, and proposed the intrinsic mechanism of different activation modes of CO_2; in addition, by constructing potential intermediates and comparing the free energy changes of each step in the whole reaction process, we determined the optimal pathway for different products, predicted the product composition based on the limiting potential, and revealed the intrinsic reaction mechanism. The results demonstrate that the loading of TM targeted to encourage CH_4 production by enhancing the coupling between TM@SnS_2 and HCOOH*, and the "charge transfer bridge" constructed by the synergistic interaction between the active center TM and substrate SnS_2 broke the scalar relationship limiting the activity and selectivity. Moreover, the binding free energy of *COOH was found to follow a "volcano curve" with the limiting potential of CO_2 reduction to CH_4, which can be used as a reliable criterion to evaluate the CO_2ER performance of TM@SnS_2.

[1]State Key Laboratory of Photocatalysis on Energy and Environment, College of Chemistry, Fuzhou University, Fuzhou 350108, People's Republic of China
[2]Fujian Provincial Key Laboratory of Theoretical and Computational Chemistry, Xiamen, Fujian 361005, People's Republic of China
[3]Lead contact
*Correspondence: zhangyf@fzu.edu.cn (Y.Z.), wlin@fzu.edu.cn (W.L.)
https://doi.org/10.1016/j.isci.2024.109658

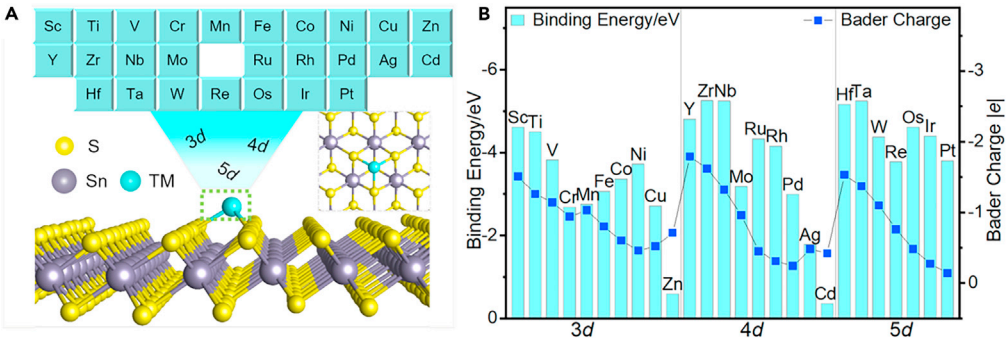

Figure 1. Configuration, energy, and Bader charge of TM@SnS_2

(A) The optimized structures of TM@SnS_2 for fcc site loading.

(B) Binding energy of TM@SnS_2 and the Bader charge of TM after loading, in which the negative value represents the electron loss.

RESULTS AND DISCUSSION

Structural features and properties

The two-dimensional 1T-SnS_2 is characterized by Sn sandwiched between two S atomic layers. Non-polar 1T-SnS_2 surface makes it difficult for electrons to inject into the $2\pi_u$ orbital of the CO_2, hence CO_2 preserves natural linear shape with physisorption energy of only −0.15 eV. The strong *sp* hybridization that exists in carbon atom cannot be easily broken by physisorption.

The substrate SnS_2 influences the binding of the active center to the intermediate by modulating the electronic structure of TM. In order to enhance the CO_2 activation on the catalyst and modify the catalytic performance, 26 types of TM single atom shown in Figure 1A were modified on SnS_2 to obtain two types of catalysts. One is TM-doped SnS_2 with TM replacing a Sn atom (Figure S1A), the other loads TM on substrate SnS_2, named TM@SnS_2, while TM has three possible loading sites including fcc, hcp, and top sites (Figures S1B and S1C). We load the TM directly at the fcc site (Figure 1A, TM dimerization at SnS_2 requires migration from one cavity to another with high energy barriers, ensuring TM dispersion in Figures S1D and S1E).[21,22] However, the binding energy of the two types of catalysts (Figure S2, and Table S1) indicates that the synthesis of TM-doped SnS_2 is energetically unfavorable. Most importantly, the SnS_2 surface remains nonpolar after doping, resulting in a weaker trapping ability of TM-doped SnS_2 for CO_2 adsorption (the poor binding of the molecule to the material confines the product to 2*e* HCOOH, which is difficult to deeply reduce). Hence, we have focused in this work on the TM@SnS_2 for fcc site loading about the CO_2ER reaction in detail.

To have a more intuitive understanding on the structure of TM@SnS_2, the deviation of the horizontal location of TM from the fcc center in TM@SnS_2 and the longitudinal distance from the surface are presented in Figure S3. The deviation of TM when loaded at the SnS_2 fcc site is about 25% on average, with a slightly higher deviation of Hf. And the longitudinal distance from the surface is distributed around 1.0–1.3 Å, while the distance of Cd from the S surface is further away, reaching about 2 Å. The full arrangement of 4*d* orbitals weakens the orbital interactions between Cd and SnS_2, resulting in poor bonding ability between Cd and the substrate SnS_2. In addition to reflecting the stability of catalysts, the coupling strength between TM and substrate also significantly affects the effectiveness of catalysis (Figure 1B). The binding of TM and SnS_2 is quite strong when the *d* orbitals are less occupied, but with the increasing number of *d* electrons, the binding energy generally declines. Interestingly, when TM is Cr (3*d*), Mn (3*d*), Mo (4*d*), Re (5*d*), etc., the coupling between *d* orbitals and SnS_2 weakens, which is attributed to the semi-filled d^5 orbitals, resulting in a decrease of binding strength, so that Cu, Ag, Zn, and Cd with d^{10} orbitals have the lowest binding energy to SnS_2. The *p* orbitals of S are dispersed near the Fermi energy level, resulting in interactions with TM *d* orbitals (Figure S4). Apart from that, the increasing number of *d* electrons is accompanied by the gradual filling of the *d* orbitals, and the lowering antibonding state energy level weakens the coupling between TM and SnS_2. Therefore, TM with lower *d* energy levels away from the Fermi level is more inclined to provide *s* orbitals participation in partial hybridization (Figures S4J and S4I), which adds the difficulty of electron transfer and intuitively manifests itself in poor binding and less charge transfer (Figure 1B, and Table S1). Moreover, the charge transferred from TM to SnS_2 has a scaling relationship with the workfunction of the TM@SnS_2 (Figure S5). With the intensified interaction between TM and SnS_2, $TM^{\sigma+}$ becomes more positive together with a decrease in the workfunction. TM reduces the minimum energy of electron spillover from catalyst, which is undoubtedly crucial for inert CO_2 capture and also implies an impact on the subsequent reaction mechanism and limiting potential (U_L).

CO_2 adsorption and activation

CO_2 capture plays an important role in carbon reduction catalytic reactions. As mentioned previously, CO_2 can only have a physisorption on pure SnS_2 without being effectively activated, and the first protonation requires energy of at least 1.47 eV, limiting further CO_2 reduction reaction (Figure S6). The adsorbed CO_2 always remain liner at a distance of 2.99 Å from the surface, with physisorption energy of only −0.15 eV. According to Norskov et al.,[23–26] the catalyst itself has a certain adsorption capacity for molecules, with a correlation between the strength of adsorption for reactants and products, suggesting that catalysts with poor CO_2 adsorption are also hard to bind with HCOOH* intermediates. In contrast to engaging in proton coupling and electron transfer (PCET), HCOOH* is easier to desorb directly, arguing for the previously

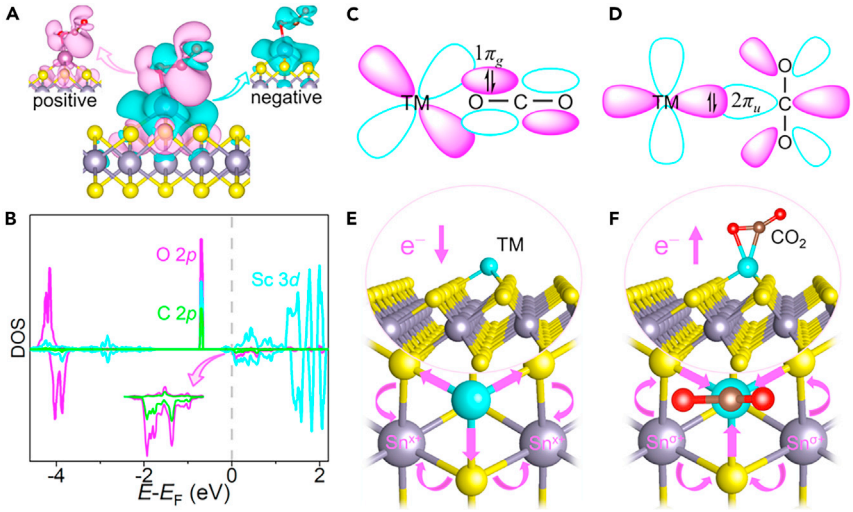

Figure 2. The electronic properties of CO_2 adsorbed on TM@SnS_2

(A) Charge density difference of CO_2 adsorbed on Sc@SnS_2 with the isovalue is set to 6 × 10^{-4} *e* $Å^{-3}$.

(B) Density of states of Sc@SnS_2.

(C and D) Mechanism of CO_2 binding to surface TM when the adsorption configuration is α1 or α2. Schematic diagram of net electron flow when (E) TM loading on SnS_2 and (F) CO_2 adsorbed on TM in α1 or α2.

reported SnS_2 as a typical formate catalyst. As a direct active site for adsorption and reduction of the catalyst, TM enhances the activation of CO_2 greatly. And crucially, the enhanced binding energy of TM@SnS_2 to HCOOH* makes it possible to synthesize 8*e* CH_4. Based on the correlation of CO_2, HCOOH, and CH_4 adsorption on TM@SnS_2 (Figure S7; Tables S2 and S3), the overall trend in adsorption energies remains consistent, with the pre-transition cycle of Hf-, Ta-, and Sc-loaded SnS_2 exhibiting relatively strong adsorption energy. However, the bonding between CO_2/HCOOH and TM@SnS_2 is mainly through TM−O, while CH_4 combines with TM@SnS_2 to form a weak TM−C bond. Therefore, the adsorption energy of CH_4 has a weak linear correlation with CO_2, and the relatively narrow CH_4 adsorption energy interval further leads to the dispersion of CH_4 adsorption energy.

Interestingly, the CO_2 configuration adsorbed on the TM@SnS_2 surface shows certain regularity (Figure S8A), in which most of the TMs and CO_2 bond as a C-TM-O bidentate ligand with a "V shape CO_2" (Figure S8B). With the increasing number of *d* electrons, the coupling between TM and C is gradually enhanced and the TM-O bond is gradually elongated (Figure S8A from α1 to α2). However, it does not apply to TM with d^5 (Cr), d^{10} (Cu, Zn, Pd, Ag, Cd), which rely on monodentate TM-O and retain the linear configuration of CO_2 (α3 in Figure S8A).

It is obvious that *d* orbitals of TM have a significant effect on CO_2 activation. Molecular and surface interaction causes energy level splitting. The position of new antibonding state can be predicted by *d* band center of TM to judge the stability of the adsorbate.[27,28] Spin down electronic states tend to have higher energy levels,[29,30] which can be used to describe the strength of the interaction between the spin-polarized TM and the adsorbate, and it was also verified by our calculations (Figure S4). Apparently, there is no correlation between the spin down *d* band center of TM and the reactants CO_2 or possible products HCOOH and CH_4 (Figure S9). However, Figure S7 illustrates that as the interaction between CO_2 and TM@SnS_2 increases, so does the adsorption energy of HCOOH and CH_4, implying that the substrate SnS_2 has a great influence on CO_2 activation.

The difference in the binding morphology (α1, α2, and α3) of TM and CO_2 is due to different bonding mechanisms. In the case of bidentate adsorption (e.g., TM = Sc), the significant electron transfer between CO_2 and TM@SnS_2 (Figure 2A), accompanied by strong hybridization between the *d* orbitals of TM and 2*p* orbitals of C/O (Figures 2B, S10A, and S10B), exposes the intense interaction of CO_2 and TM@SnS_2. TM with empty *d* orbitals can accommodate electrons from the highest occupied orbital ($1\pi_g$) of CO_2 (Figure 2C), while TM feeds back electrons to the lowest unoccupied orbital ($2\pi_u$) of the CO_2 (Figure 2D), resulting in an eventual electron gain for CO_2. According to the Bader charge calculations (Table S3), the charge changes of TM are negligible before and after CO_2 adsorption. When loading on SnS_2, TM exhibits electron loss (Table S1). On application of the cathodic potential, it gains additional electrons through the TM-S bond as "charge transfer bridge" firstly, and the reduced TM then provides electrons for CO_2. Hence, we can observe the accumulation and loss of charge between the substrate and TM in Figure 2A. In the aforementioned processes, Sn achieves a transition of $Sn^{4+} \rightarrow Sn^{x+} \rightarrow Sn^{\sigma+}$ ($2 < x < \sigma < 4$) (Figures 2E and 2F), as shown in the studies of Huang et al.[31,32] Transition metal with fewer *d*-occupied orbitals has a powerful interaction with the SnS_2 (Figure 1B) that prevents the formation of the reduced state, and the lack of electrons causes the activation of CO_2 to take on the α1 mode where TM is intensely coupled with O than C. Monodentate adsorption (α3) presents another bonding mechanism. In this case, weak interaction exists between TM and CO_2 (e.g., TM = Cr, Cu). Due to the relative inertness of the *d* orbital with a special electron arrangement (d^5, d^{10}), TM provides *s* orbital hybridization with the 2*p* orbital of O additionally (Figures S10C and S10D). The strong electronegativity prevents the generation of TM reduced state, and SnS_2 accepts few electrons from CO_2 using the TM-S bond as "charge transfer bridge" (Figures S10E–S10G) to realize $Sn^{4+} \rightarrow Sn^{x+} \rightarrow Sn^{\sigma+}$, where $2 < \sigma < x < 4$. At this moment, the highest occupied orbital ($1\pi_g$) of CO_2 transfers

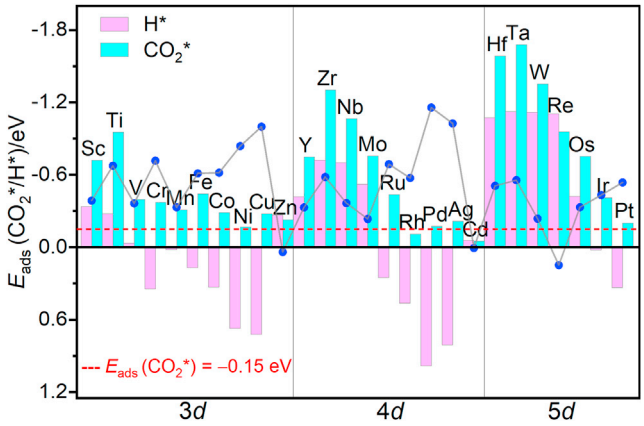

Figure 3. Adsorption energy of CO_2* and H* on TM@SnS_2, where the blue dots are the difference in adsorption energy between them, i.e., E_{ads} (CO_2*) − E_{ads} (H*) and the red dashed line represents the CO_2 adsorption energy on pure SnS_2

electrons to the empty *s* orbital (Figure S11A), and TM *d* orbital feeds back electrons to the lowest unoccupied orbital ($2\pi_u$) of CO_2 (Figure S11B). Note that, unlike the lower energy levels of d^{10}, the Cr *d* orbitals are distributed near the Fermi energy level and it disperses to a certain extent in CO_2 adsorption. In conclusion, these two activation mechanisms reveal that CO_2 activation is synergistically facilitated by "charge transfer bridge" between TM and SnS_2. This is equivalent to the "electron sponge" proposed by Su et al.[33] We observed similar effect with Fe-N_4-C catalyst in CO_2ER,[34] while the multivalent state of Sn in the substrate SnS_2 facilitates the electron transfer even more than in graphite. Overall, we have explained the synergistic interaction between TM and substrate to promote the activation of CO_2 and further regulate the coupling strength of intermediates and TM@SnS_2 from a deep electron supply relationship.

The exotherm of CO_2 adsorption on the TM@SnS_2 increases with the period of TM, and CO_2 adsorption is enhanced by loading SnS_2 with pre-transition metals (Sc, Ti, Zr, Hf, Ta, W, etc.) for each period (Figure 3). CO_2 adsorption energy of most TM@SnS_2 is stronger than that of pure SnS_2, with the exception of Rh@SnS_2 and Cd@SnS_2 (−0.11 and −0.05 eV). In combination with the adsorption correlation aforementioned (Figure S7A), the poor binding of CO_2 to Rh@SnS_2 and Cd@SnS_2 adds to the difficulty of selectively generating CH_4 from CO_2ER. Furthermore, it is crucial to prevent the poisoning of H* at the monatomic active site. Re@SnS_2, Zn@SnS_2, and Cd@SnS_2 exhibit superiority of H* binding and hinder CO_2 adsorption. In summary, comparing the CO_2 adsorption energy on TM@SnS_2 with that on pure SnS_2 and the competition with H*, we ignored the investigation of CO_2 reduction performance for Rh@SnS_2, Re@SnS_2, Zn@SnS_2, and Cd@SnS_2 and only considered the remaining 22 TM@SnS_2.

Mechanisms and selectivity of reactions

Competition between COOH/HCOO* and H**

The independent active site of TM@SnS_2 blocks the C−C coupling and ensures that CO_2 is reduced solely to C1 product.[35] We complement the potential reaction pathways for of CO_2ER proposed by Yuan et al. (Scheme S1).[36] CO_2 is progressively hydrogenated to HCOOH or CH_4 *via* PCET steps, with 35 possible radical reactions (Supporting Information R1-R35). The Gibbs free energy change for all reactions in the pathway was calculated (Supporting Information ES1-E35, Figure S12) to obtain the U_L for the CO_2ER. Brønsted-Evans-Polanyi relationship shows that lower Gibbs free energy change implies a smaller thermodynamic potential for the reaction.[37,38] As a side reaction of CO_2 reduction, not only the hydrogen reduction reaction (HER) reduces the Faraday efficiency, but the competing depletion of proton and electron pairs from electrolyte near the cathode also substantially slows the rate of CO_2 conversion. During the initial step of CO_2 hydrogenation, the proton may bond with O to form *COOH or transfer to C to generate HCOO* intermediates. ΔG (COOH*/HCOO*) and ΔG (H*) reflect the competition between CO_2ER and HER (Figure 4A). All of HCOO* and most of COOH* intermediates exhibit energetic superiority over H*, but the COOH* intermediates of TM@SnS_2 (TM = Ta, W, Os, Mn, Cu, Ag) require slightly higher energies than H*. The independent active sites are occupied by COOH* and HCOO*, inhibiting the occurrence of hydrogen precipitation side reactions and allowing TM@SnS_2 to exhibit superiority for CO_2ER. During the reaction, with similar surface adsorption bonds, there is a linear scalar relationship through the C-bound and O-bound intermediates, respectively.[23] In TM@SnS_2, the *COOH binding free energies bound to TM *via* C as a monodentate ligand and HCOO* bound by the bidentate ligand O-TM-O are also heavily correlated (Figure 4B), with HCOO* having a lower energy compared to COOH*. The scaling relationship between HCOO* and HCOOH* diverging due to the weaken TM-O bond between the HCOOH* and TM (Figure S13). There is a poor correlation between the binding energies of the other subsequent intermediates. The scaling relationship imposes certain limitations on activity and selectivity in the involvement of transition metals in CO_2ER, which are broken by the "charge transfer bridge" between TM and SnS_2.

Production of 2e HCOOH

CO_2 can form HCOOH* intermediates after two-step PCET, then HCOOH desorbed from surface with the relevant energy changes represented in Table S4. Figures 5A–5C show the free energy diagrams of HCOOH production after TM loading for 3*d*, 4*d*, and 5*d* periods,

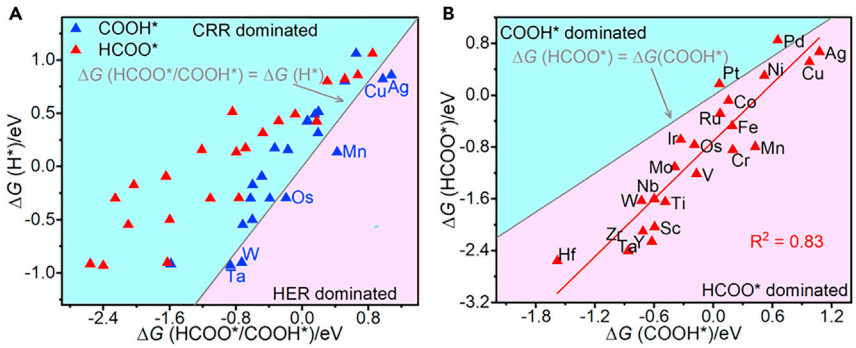

Figure 4. The relationship with the free energies of reaction intermediates

(A) Binding free energy competition between COOH*/HCOO* and H* intermediates.

(B) Comparison of the binding free energy of COOH* and HCOO*.

respectively, with *HCOO or COOH* intermediates being produced in the first step. On the one hand, the lower *HCOO energy increases the difficulty of converting *HCOO to *HCOOH, resulting in most TM@SnS_2 to yield formic acid through *COOH; on the other hand, the "charge transfer bridge" between TM and SnS_2 enlarges the coupling strength between TM and *HCOOH, making HCOOH desorption more difficult. The representative TMs are listed in Figure 5D. HCOOH* trapped on the surface through strong TM-O bonds is instead more readily hydrogenated and involved in reduction reactions than in desorption. The post-transition metals seem to exhibit high activity for HCOOH production, but the selectivity of CO_2ER depends on the difference in the limiting potential between the various products.

Production of 8e CH_4 and the "volcano curve"

Based on Scheme S1 and R1-R35 (Supporting Information), Gibbs free energy changes were calculated for 35 radical reactions (Figure S12). We can roughly see that in the hydrogenation of CO_2 to CH_4, the former part of the reduction (i.e., 1-4e) is more endothermic, while the latter part is mainly exothermic. In addition, R1 and R2 of 1e exhibits a tendency of increasing free energy change in each period; however, R34 and R35 of 8e show a gradual decline in energy change. The relatively insignificant variation in the middle part reaction and the limited linear scaling relationship favor the improved activity of the TM@SnS_2.

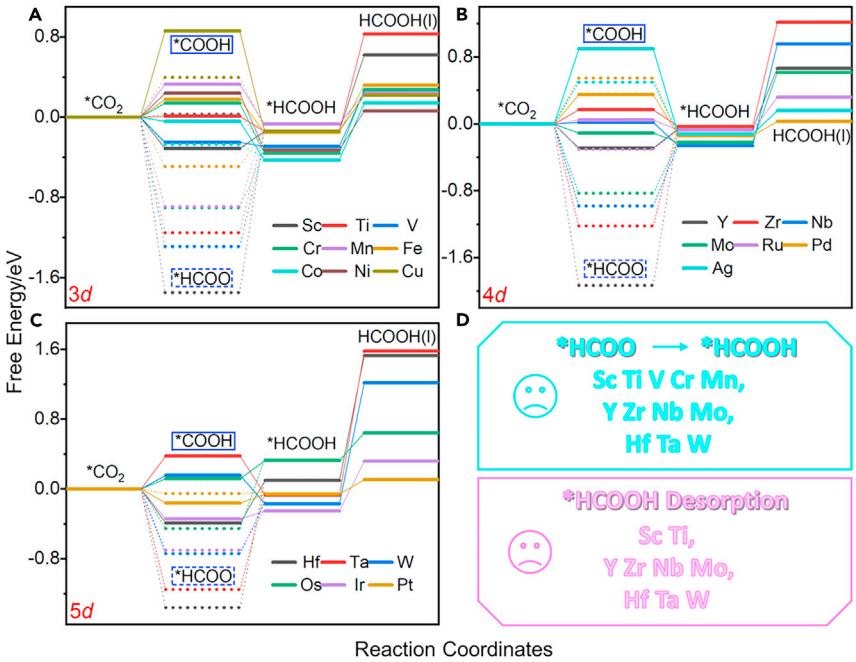

Figure 5. The free energies of HCOOH generated on TM@SnS_2

Free energy diagrams of HCOOH production of TM@SnS_2 for (A) 3*d*, (B) 4*d*, and (C) 5*d* periods. The solid line is the energy of *COOH while the dashed line refers to *HCOO.

(D) Two unfavorable processes of HCOOH formation and the corresponding TMs for each step.

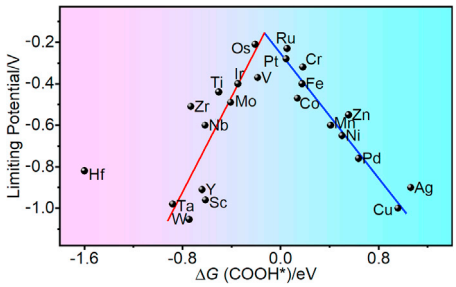

Figure 6. The "volcano curve" between ΔG (*COOH) and the limiting potential U_L (CH_4)

We screened the lowest energy pathway for CH_4 production from TM@SnS_2 (Figures S14 and S15) and obtained the U_L for CH_4 from CO_2ER. As aforementioned, while *HCOO is more energetically favorable than *COOH, it requires more energy to continue hydrogenation. Therefore most TMs (except Ni, Cu, Ta, Pt) get the lowest energy path for CH_4 generation *via* *COOH intermediate. We explored the relationship regarding the CO_2 adsorption energy and the *COOH binding energy of TM@SnS_2 relative to the U_L of the CH_4 production (Figure S16A) and found that the spontaneous adsorption of CO_2 simply acts as a knockon for reaction to take place and has almost no effect on activity of CH_4. And the corresponding CH_4 activity exhibits an advantage when the binding energy of *COOH remains between −0.4 and 0.2 eV. Furthermore, there is a correlation between ΔG (R35) and *COOH binding free energy, with a better activity when ΔG (R35) is in −0.6 to 0.2 eV (Figure S16B). The Sabatier principle suggests that the bond between the reaction intermediate and the catalyst should be neither too strong nor too weak in order to obtain the best catalytic performance.[39] There is indeed a "volcano curve" about ΔG (*COOH) and the U_L (CH_4) in our system (Figure 6); when ΔG (*COOH) < −0.4 eV, the binding between *COOH and TM@SnS_2 is too strong to proceed with hydrogenation, mainly in the pre-transition metal. Unexpectedly, Hf is farther away from SnS_2, making it overcoupled to COOH* and departing from the volcano curve. While ΔG (*COOH) > 0.2 eV, *COOH formation becomes an endothermic process with a weak coupling, mostly distributed in the post-transition metal. Only if −0.4 eV < ΔG (*COOH) < 0.2 eV, TM@SnS_2 has a limited potential for CO_2ER at the "volcano top" with significant CH_4 activity. In particular, Cr of 3*d*, Ru of 4*d*, as well as Os and Pt in 5*d* periods have excellent catalytic activity. Considering the tradeoff between the actual environment of electroreduction and computational pressure, we compared the free energy change of them before and after imposed implicit solvation model (Figure S15, and Table S5). With hydrogen bonding constraints, the energy of the H_2O molecule corrected by the implicit solvent model decreases by 0.31 eV, resulting in a slight energy decrease in the elementary reaction involving the removal of H_2O after one-step PCET. However, the overall free energy change of the elementary reaction is consistent, along with a subtle decrease in the limiting potential of the reaction.

Anticipated products of CO_2ER

In previous subsection, we have investigated the mechanism of CO_2 reduction to produce HCOOH and CH_4, exploring the optimal pathways about them. The ΔG_{MAX} about reaction reveals the catalytic activity of both products in the CO_2ER ultimately in Figure 7. The monoatomic loading enhances the coupling of *HCOOH to TM@SnS_2 and hinders HCOOH desorption. Overall, the U_L (HCOOH) is more negative relative to CH_4 production, with the former transition metal being more apparent in 4*d* and 5*d*, and the difference between the U_L reflecting the selectivity of the products. Sc and Y as pre-transition metals, Ni, Cu, Pd, Ag, Pt, as post-transition metals, and Mn are more superior for HCOOH synthesis and most TMs require less energy for CH_4 production. Of these TMs, Ti, Cr, Zr, Nb, Mo, Hf, Ta, and W have superior CH_4 selectivity with a larger difference in U_L. Finally, with its lower ΔG_{MAX} (0.32 eV) and excellent selectivity, Cr@SnS_2 is quite a promising catalyst for the formation of CH_4 in CO_2ER.

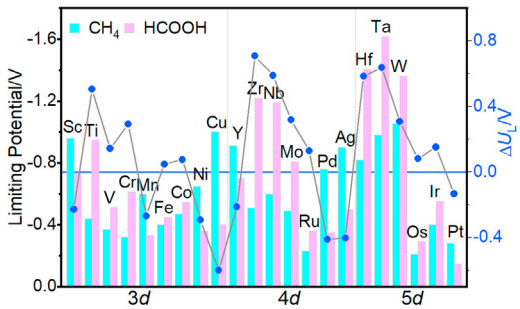

Figure 7. Limiting potential for CO_2ER to HCOOH and CH_4 on TM@SnS_2, the blue dots are the difference in U_L between them, i.e., U_L (CH_4) − U_L (HCOOH), where the blue line represents U_L (CH_4) = U_L (HCOOH)

Conclusion

In conclusion, the TM@SnS_2 makes full use of the functional synergy between the TM and substrate, which strengthens the coupling between the intermediate and catalyst through "charge transfer bridge" effectively. Not only does it have a superior CO_2 adsorption capacity than pure SnS_2, but also TM@SnS_2 tends to reduce CO_2 to high-value CH_4 compared to conventional SnS_2, and which is limited to 2*e* HCOOH production. Our calculations indicate that with high selectivity and excellent CO_2ER performance, economical Cr@SnS_2 near the "volcano top" is an efficient catalyst for CH_4 production, and implicit solvation measurement did not significantly affect the limiting potential. This work provides valuable insights into the efficient design of single-atom electrocatalysts targeted to obtain desired products, and it is hoped that the aforementioned work will contribute to the further development of experimental and theoretical studies.

Limitations of the study

We have carried out a theoretical study of TM@SnS_2 for CO_2 reduction reaction. However, the reaction intermediates are susceptible to the influence of solvents in the microscopic state and the voltage under real reaction conditions, etc. The interactions between the catalyst, adsorbent, and electrolyte and the relationship between the reaction performance and the potential were not sufficiently considered in this work.

STAR★METHODS

Detailed methods are provided in the online version of this paper and include the following:

- KEY RESOURCES TABLE
- RESOURCE AVAILABILITY
  - Lead contact
  - Materials availability
  - Data and code availability
- EXPERIMENTAL MODEL AND STUDY PARTICIPANT DETAILS
- METHOD DETAILS
- QUANTIFICATION AND STATISTICAL ANALYSIS

SUPPLEMENTAL INFORMATION

Supplemental information can be found online at https://doi.org/10.1016/j.isci.2024.109658.

ACKNOWLEDGMENTS

This work was financially supported by the National Natural Science Foundation of China (21973014, 21773030, and 22250710676).

AUTHOR CONTRIBUTIONS

Y.K. and J.P. performed the computation. Y.K. wrote the manuscript. W.L. and Y.K. designed the project and revised the manuscript. All authors were involved in the general discussion. The manuscript was written through contributions of all authors. All authors have given approval to the final version of the manuscript.

DECLARATION OF INTERESTS

The authors declare that they have no known competing financial interests or personal relationships that could have appeared to influence the work reported in this paper.

Received: December 11, 2023
Revised: February 29, 2024
Accepted: April 1, 2024
Published: April 3, 2024

REFERENCES

1. Keith, D.W. (2009). Why Capture CO_2 from the Atmosphere? Science *325*, 1654–1655.
2. Allen, M.R., Frame, D.J., Huntingford, C., Jones, C.D., Lowe, J.A., Meinshausen, M., and Meinshausen, N. (2009). Warming Caused by Cumulative Carbon Emissions Towards the Trillionth Tonne. Nature *458*, 1163–1166.
3. Ola, O., and Maroto-Valer, M. (2015). Review of Material Design and Reactor Engineering on TiO_2 Photocatalysis for CO_2 Reduction. J. Photochem. Photobiol. C Photochem. Rev. *24*, 16–42.
4. Omer, A.M. (2008). Energy, Environment and Sustainable Development. Renew. Sustain. Energy Rev. *12*, 2265–2300.
5. Kong, Y., Li, Y., Zhang, Y., and Lin, W. (2021). Unveiling the Selectivity of CO_2 Reduction on Cu_2ZnSnS_4: The Effect of Exposed Termination. J. Phys. Chem. C *125*, 24967–24973.
6. Kim, D., Resasco, J., Yu, Y., Asiri, A.M., and Yang, P. (2014). Synergistic Geometric and Electronic Effects for Electrochemical Reduction of Carbon Dioxide using Gold–copper Bimetallic Nanoparticles. Nat. Commun. *5*, 4948.
7. Gao, S., Lin, Y., Jiao, X., Sun, Y., Luo, Q., Zhang, W., Li, D., Yang, J., and Xie, Y. (2016).

Partially Oxidized Atomic Cobalt Layers for Carbon Dioxide Electroreduction to Liquid Fuel. Nature *529*, 68–71.
8. Graves, C., Ebbesen, S.D., Mogensen, M., and Lackner, K.S. (2011). Sustainable Hydrocarbon Fuels by Recycling CO_2 and H_2O with Renewable or Nuclear Energy. Renew. Sustain. Energy Rev. *15*, 1–23.
9. Turner, J.A. (1999). A Realizable Renewable Energy Future. Science *285*, 687–689.
10. Liu, J. (2017). Catalysis by Supported Single Metal Atoms. ACS Catal. *7*, 34–59.
11. Liu, J., Kong, X., Zheng, L., Guo, X., Liu, X., and Shui, J. (2020). Rare Earth Single-Atom Catalysts for Nitrogen and Carbon Dioxide Reduction. ACS Nano *14*, 1093–1101.
12. Gong, L., Zhang, D., Lin, C.-Y., Zhu, Y., Shen, Y., Zhang, J., Han, X., Zhang, L., and Xia, Z. (2019). Catalytic Mechanisms and Design Principles for Single-Atom Catalysts in Highly Efficient CO_2 Conversion. Adv. Energy Mater. *9*, 1902625.
13. Ji, S., Li, Y., Zhang, Y., and Lin, W. (2023). Computational Screening of High Activity and Selectivity of CO_2 Reduction *via* Transition Metal Single-Atom Catalysts on Triazine-based Graphite Carbon Nitride. Phys. Chem. Chem. Phys. *25*, 24022–24030.
14. Ju, L., Tan, X., Mao, X., Gu, Y., Smith, S., Du, A., Chen, Z., Chen, C., and Kou, L. (2021). Controllable CO_2 Electrocatalytic Reduction *via* Ferroelectric Switching on Single Atom Anchored In_2Se_3 Monolayer. Nat. Commun. *12*, 5128.
15. Zhang, A., He, R., Li, H., Chen, Y., Kong, T., Li, K., Ju, H., Zhu, J., Zhu, W., and Zeng, J. (2018). Nickel Doping in Atomically Thin Tin Disulfide Nanosheets Enables Highly Efficient CO_2 Reduction. Angew. Chem. Int. Ed. *57*, 10954–10958.
16. Chen, T., Liu, T., Ding, T., Pang, B., Wang, L., Liu, X., Shen, X., Wang, S., Wu, D., Liu, D., et al. (2021). Surface Oxygen Injection in Tin Disulfide Nanosheets for Efficient CO_2 Electroreduction to Formate and Syngas. Nano-Micro Lett. *13*, 189.
17. Chen, M., Wan, S., Zhong, L., Liu, D., Yang, H., Li, C., Huang, Z., Liu, C., Chen, J., Pan, H., et al. (2021). Dynamic Restructuring of Cu-Doped SnS_2 Nanoflowers for Highly Selective Electrochemical CO_2 Reduction to Formate. Angew. Chem. Int. Ed. *60*, 26233–26237.
18. Woldu, A.R., Talebi, P., Yohannes, A.G., Xu, J., Wu, X.-D., Siahrostami, S., Hu, L., and Huang, X.-C. (2023). Insights into Electrochemical CO_2 Reduction on SnS_2: Main Product Switch from Hydrogen to Formate by Pulsed Potential Electrolysis. Angew. Chem. Int. Ed. *62*, e202301621.
19. Woldu, A.R., Huang, Z., Zhao, P., Hu, L., and Astruc, D. (2022). Electrochemical CO_2 Reduction (CO_2RR) to Multi-carbon Products over Copper-based Catalysts. Coord. Chem. Rev. *454*, 214340.
20. Zhao, Y., Zhang, X.-G., Bodappa, N., Yang, W.-M., Liang, Q., Radjenovica, P.M., Wang, Y.-H., Zhang, Y.-J., Dong, J.-C., Tian, Z.-Q., and Li, J.F. (2022). Elucidating Electrochemical CO_2 Reduction Reaction Processes on Cu(*hkl*) Single-crystal Surfaces by *in situ* Raman Spectroscopy. Energy Environ. Sci. *15*, 3968–3977.
21. Wan, Q., Chen, X., and Gui, Y. (2020). First-Principles Insight into a Ru-Doped SnS_2 Monolayer as a Promising Biosensor for Exhale Gas Analysis. ACS Omega *5*, 8919–8926.
22. Xia, F., and Yang, F. (2022). SnS_2 Monolayer-Supported Transition Metal Atoms as Efficient Bifunctional Oxygen Electrocatalysts: A Theoretical Investigation. Energy Fuels *36*, 4992–4998.
23. Abild-Pedersen, F., Greeley, J., Studt, F., Rossmeisl, J., Munter, T.R., Moses, P.G., Skúlason, E., Bligaard, T., and Nørskov, J.K. (2007). Scaling Properties of Adsorption Energies for Hydrogen-Containing Molecules on Transition-Metal Surfaces. Phys. Rev. Lett. *99*, 016105.
24. Nørskov, J.K., Bligaard, T., and Kleis, J. (2009). Rate Control and Reaction Engineering. Science *324*, 1655–1656.
25. Khorshidi, A., Violet, J., Hashemi, J., and Peterson, A.A. (2018). How Strain can Break the Scaling Relations of Catalysis. Nat. Catal. *1*, 263–268.
26. Nørskov, J.K., Abild-Pedersen, F., Studt, F., and Bligaard, T. (2011). Density Functional Theory in Surface Chemistry and Catalysis. Proc. Natl. Acad. Sci. USA *108*, 937–943.
27. Hammer, B., and Nørskov, J. (1995). Electronic Factors Determining the Reactivity of Metal Surfaces. Surf. Sci. *343*, 211–220.
28. Hammer, B., and Nørskov, J.K. (2000). Theoretical Surface Science and Catalysis—calculations and Concepts. Adv. Catal. *45*, 71–129.
29. Liu, J.-C., Ma, X.-L., Li, Y., Wang, Y.-G., Xiao, H., and Li, J. (2018). Heterogeneous Fe_3 Single-cluster Catalyst for Ammonia Synthesis *via* an Associative Mechanism. Nat. Commun. *9*, 1610.
30. Gao, G., Waclawik, E.R., and Du, A. (2017). Computational Screening of Two-dimensional Coordination Polymers as Efficient Catalysts for Oxygen Evolution and Reduction Reaction. J. Catal. *352*, 579–585.
31. Liu, S., Yang, H.B., Hung, S.-F., Ding, J., Cai, W., Liu, L., Gao, J., Li, X., Ren, X., Kuang, Z., et al. (2020). Elucidating the Electrocatalytic CO_2 Reduction Reaction over a Model Single-Atom Nickel Catalyst. Angew. Chem. Int. Ed. *59*, 798–803.
32. Wang, Y.-R., Huang, Q., He, C.-T., Chen, Y., Liu, J., Shen, F.-C., and Lan, Y.-Q. (2018). Oriented Electron Transmission in Polyoxometalate-metalloporphyrin Organic Framework for Highly Selective Electroreduction of CO_2. Nat. Commun. *9*, 4466.
33. Zhao, C., Su, X., Wang, S., Tian, Y., Yan, L., and Su, Z. (2022). Single-atom Catalysts on Supported Silicomolybdic Acid for CO_2 Electroreduction: a DFT Prediction. J. Mater. Chem. A *10*, 6178–6186.
34. Cao, H., Zhang, Z., Chen, J.-W., and Wang, Y.-G. (2022). Potential-Dependent Free Energy Relationship in Interpreting the Electrochemical Performance of CO_2 Reduction on Single Atom Catalysts. ACS Catal. *12*, 6606–6617.
35. Moses-DeBusk, M., Yoon, M., Allard, L.F., Mullins, D.R., Wu, Z., Yang, X., Veith, G., Stocks, G.M., and Narula, C.K. (2013). CO Oxidation on Supported Single Pt Atoms: Experimental and ab Initio Density Functional Studies of CO Interaction with Pt Atom on θ-Al_2O_3(010) Surface. J. Am. Chem. Soc. *135*, 12634–12645.
36. Yuan, H., Li, Z., Zeng, X.C., and Yang, J. (2020). Descriptor-Based Design Principle for Two-Dimensional Single-Atom Catalysts: Carbon Dioxide Electroreduction. J. Phys. Chem. Lett. *11*, 3481–3487.
37. Evans, M.G., and Polanyi, M. (1938). Inertia and Driving Force of Chemical Reactions. Trans. Faraday Soc. *34*, 11–24.
38. Bronsted, J.N. (1928). Acid and Basic Catalysis. Chem. Rev. *5*, 231–338.
39. Sabatier, P. (1911). Hydrogénations et déshydrogénations par catalyse. Ber. Dtsch. Chem. Ges. *44*, 1984–2001.
40. Kresse, G., and Furthmüller, J. (1996). Efficient Iterative Schemes for *ab initio* Total-energy Calculations using a Plane-wave Basis Set. Phys. Rev. B *54*, 11169–11186.
41. Perdew, J.P., Burke, K., and Ernzerhof, M. (1996). Generalized Gradient Approximation Made Simple. Phys. Rev. Lett. *77*, 3865–3868.
42. Kresse, G., and Joubert, D. (1999). From Ultrasoft Pseudopotentials to the Projector Augmented-wave Method. Phys. Rev. B *59*, 1758–1775.
43. Sanville, E., Kenny, S.D., Smith, R., and Henkelman, G. (2007). Improved Grid-based Algorithm for Bader charge Allocation. J. Comput. Chem. *28*, 899–908.
44. Henkelman, G., Arnaldsson, A., and Jónsson, H. (2006). A Fast and Robust Algorithm for Bader Decomposition of Charge Density. Comput. Mater. Sci. *36*, 354–360.
45. Grimme, S., Ehrlich, S., and Goerigk, L. (2011). Effect of the Damping Function in Dispersion Corrected Density Functional Theory. J. Comput. Chem. *32*, 1456–1465.
46. Bengtsson, L. (1999). Dipole Correction for Surface Supercell Calculations. Phys. Rev. B *59*, 12301–12304.
47. Mathew, K., Sundararaman, R., Letchworth-Weaver, K., Arias, T.A., and Hennig, R.G. (2014). Implicit Solvation Model for Density-Functional Study of Nanocrystal Surfaces and Reaction Pathways. J. Chem. Phys. *140*, 084106.
48. Cramer, C.J., and Truhlar, D.G. (1999). Implicit Solvation Models: Equilibria, Structure, Spectra, and Dynamics. Chem. Rev. *99*, 2161–2200.
49. Wang, X., Niu, H., Liu, Y., Shao, C., Robertson, J., Zhang, Z., and Guo, Y. (2020). Theoretical Investigation on Graphene-supported Single-atom Catalysts for Electrochemical CO_2 Reduction. Catal. Sci. Technol. *10*, 8465–8472.
50. Henkelman, G., Uberuaga, B.P., and Jónsson, H. (2000). A Climbing Image Nudged Elastic Band Method for Finding Saddle Points and Minimum Energy Paths. J. Chem. Phys. *113*, 9901–9904.
51. Henkelman, G., and Jónsson, H. (2000). Improved Tangent Estimate in the Nudged Elastic Band Method for Finding Minimum Energy Paths and Saddle Points. J. Chem. Phys. *113*, 9978–9985.

STAR★METHODS

KEY RESOURCES TABLE

REAGENT or RESOURCE	SOURCE	IDENTIFIER
Software and algorithms		
VASP code Kresse and Furthmüller[40]	VASP software GmbH	https://www.vasp.at
VESTA software package	JP-Minerals	https://jp-minerals.org/vesta/en/
VASPsol Mathew and Cramer[47,48]	Open source	https://www.opensourceagenda.com/projects/vaspsol

RESOURCE AVAILABILITY

Lead contact

Further requests for resources should be directed to and will be fulfilled by the Lead Contact, Wei Lin (wlin@fzu.edu.cn).

Materials availability

This study did not yield new unique reagents.

Data and code availability

- The published article includes all datasets generated or analyzed during this study.
- This study did not generate new code.
- Any additional information required to reanalyze the data reported in this paper is available from the lead contact upon request.

EXPERIMENTAL MODEL AND STUDY PARTICIPANT DETAILS

Our study does not use experimental models typical in the life sciences.

METHOD DETAILS

Density functional theory (DFT) calculations were carried out by the VASP package.[40] The exchange and correlation interactions were depicted by the generalized gradient approximation of Perdew, Burke, and Ernzerhof (PBE) functional.[41] Electron-ion mutual effects were modelled by using Projector augmented wave (PAW) potentials.[42] Bader analysis program[43,44] was employed to quantify the changes of electronic structure. The DFT-D3 correction was applied to assess the weak interactions.[45] Dipole correction in the z direction was opened to correct potential spurious terms brought by the asymmetry of the slabs.[46] The TM@SnS_2 was generated on a (3 × 3) SnS_2 supercell for probing the CO_2 reduction reaction mechanism. All of atoms were relaxed in any directions with the process of the structural optimization. A Monkhorst-Pack 3 × 3 × 1 k-point grid was adopted to sample the Brillouin zone during geometry optimizations, whereas a 7 × 7 × 1 k-point grid was utilized for electronic property computations. The convergence criteria for the structure relaxation were set to 0.02 eV·Å^{-1} in force and 10^{-6} eV in energy, respectively. The kinetic cut-off energy of the plane wave basis was set to 450 eV. To avoid the interactions between the neighbouring slabs, the vacuum in the surface normal direction was set to 15 Å. Implicit solvation model[47,48] (using VASPsol) taking into account the aqueous electrolyte was used to simulate the reaction environment of Cr@SnS_2, Ru@SnS_2, Os@SnS_2 and Pt@SnS_2.

The binding energy was calculated by:

$$E_b = E(\mathrm{TM@SnS_2}) - E(\mathrm{TM}) - E(\mathrm{SnS_2}) \quad \text{(Equation 1)}$$

Where E(TM@SnS_2), E(TM) and E(SnS_2) denote the total energy of fcc loaded TM@SnS_2, single TM and pure SnS_2.And the adsorption energy of molecular (CO_2, HCOOH and CH_4) was calculated by:

$$E_{ads} = E(\mathrm{mol - TM@SnS_2}) - E(\mathrm{mol}) - E(\mathrm{TM@SnS_2}) \quad \text{(Equation 2)}$$

E(mol-TM@SnS_2), E(mol) refer to the energies of the system after molecular adsorption and the individual molecular, respectively. Deviation χ of the horizontal location of TM was calculated by:

$$\chi = \left(1 - \frac{\sqrt{d_{TM-S}^2 - H^2}}{d_{Sn-S}}\right) \times 100\% \quad \text{(Equation 3)}$$

Where $d_{TM\text{-}S}$ and $d_{Sn\text{-}S}$ represent the average distance of TM-S and Sn-S bond below TM, and H is the longitudinal distance from the surface.[49] The free energy of a proton/electron pair ($H^+ + e^-$) is equal to half of the gaseous hydrogen (1/2H_2) at an equilibrium potential, namely the free

energy variations were calculated based on computational hydrogen electrode (CHE) model. The change of Gibbs free energy (ΔG) was computed as follows:

$$\Delta G = \Delta E + \Delta E_{ZPE} - T\Delta S + \int C_P dT \quad \text{(Equation 4)}$$

Where ΔE, ΔE_{ZPE}, ΔS and ΔG_U signify the difference value of total energy, zero potential energy, entropy, and the free energy contribution related to enthalpic temperature correction, respectively, and T is the room temperature (298.15 K). Free energy change (ΔG) of the elementary reaction represents the free energy difference between the product and reactant and the formula of ΔG specific to each step is presented below (ES1-35) in supporting information. The limiting potential (U_L) of the reaction is obtained by $U_L = -\Delta G_{MAX}/e$, where ΔG_{MAX} is the largest free energy change, corresponding to the potential determining step (PDS). The climbing image nudged elastic band (CI-NEB) method was adopted to locate the minimum-energy paths, and force convergence standard is 0.05 eV/Å.[50,51] The transition states (TSs) were verified using vibrational frequency calculations. The d band center (ε_d) is calculated by:

$$\varepsilon_d = \frac{\int n_d(\varepsilon)\varepsilon d\varepsilon}{\int n_d(\varepsilon) d\varepsilon} \quad \text{(Equation 5)}$$

The ε and $n_d(\varepsilon)$ are the electronic energy of states and the electronic density of states, respectively.

QUANTIFICATION AND STATISTICAL ANALYSIS

Calculate the variance of the adsorption energy linear relationship using Microsoft Excel.